The first offline land carbon simulation over Europe driven by the atmospheric forcing of a global storm-resolving climate model

Junhong Lee[1,*] and Cathy Hohenegger[1]

[1]Max Planck Institute for Meteorology, Hamburg, Germany

[*]Current affiliation: The research Institute of Basic Sciences, Seoul National University, Seoul, Republic of Korea

Correspondence: Junhong Lee (junhong.lee@mpimet.mpg.de; junhonglee89@gmail.com)

Abstract. This study is motivated by the hypothesis that the drizzle problem of coarse-resolution climate models, whereby convective precipitation preferentially falls as light precipitation rather than short-lived and intense storms, leads to low gross primary productivity (GPP). To test this hypothesis, we perform an offline land carbon simulation over Europe using a terrestrial biosphere model driven by atmospheric forcing from a global km-scale climate simulation with explicitly resolved convection. This simulation is compared with a coarse-resolution simulation driven by atmospheric forcing from a coarse-resolution climate model with parameterized convection. We find that shorter, more intense daily precipitation events when convection is explicitly resolved allow for stronger downward shortwave radiation on rainy days, thereby enhancing photosynthesis for a given precipitation amount. This effect is visible beyond a precipitation threshold of 14 mm day^{-1}. It also manifests itself as a steady decrease of GPP with intensifying precipitation in the coarse-resolution simulation, whereas productivity stays approximately constant in the storm-resolving simulation. The latter behavior appears closer to observations. At the same time, differences in the precipitation climatology between the two atmospheric forcing datasets, with a deficit of precipitation over Europe, and especially over central eastern Europe, in the km-scale forcing result in an overall decrease of GPP in the storm-resolving simulation. Consistent with these GPP changes, autotrophic respiration and heterotrophic respiration are smaller in the km-scale simulation, the latter firstly due to drier mean conditions. Hence, whereas explicitly resolving convection allows for enhanced productivity under strongly precipitating events, this effect is modulated by the simulated mean climate and domain-mean productivity may increase or decrease.

1 Introduction

Terrestrial ecosystems on land take up about 3.3 Gt carbon per year on average (Friedlingstein et al., 2023). In order to estimate the magnitude of the land carbon sinks, dynamic global vegetation models are widely used. These models represent the terrestrial carbon cycle processes with varying levels of complexity. Generally, they can be used in an offline mode driven by prescribed atmospheric forcing or in a fully interactive configuration within Earth System Models.

However, estimates of carbon fluxes are subject to substantial uncertainties. Previous studies have identified the representation of terrestrial and biosphere processes (model uncertainty), of land input datasets (e.g. land cover map, distribution of plant functional types) and the atmospheric forcing as potential sources of uncertainty. For example, Jung et al. (2007b) found that changes in model resolution or land-cover maps had little effect on the simulated gross primary productivity over Europe, but changes in either the terrestrial biosphere model or the atmospheric forcing significantly affected the results. In their study, uncertainties in atmospheric forcing are especially projected on interannual variations in gross primary productivity. In contrast, more recent work by Hartley et al. (2017) and Georgievski and Hagemann (2019) showed that uncertainty in the derivation of land input dataset can exert much stronger effects on climate simulations. The different resolutions, 0.25° in Jung et al. (2007b) versus about 2° in the more recent studies, might explain some of the discrepancy. Comparing model uncertainty and uncertainty in atmospheric forcing, Hardouin et al. (2022) concluded that atmospheric forcing accounts for a large fraction of uncertainty in the variability of gross primary productivity (75%) and autotrophic respiration (90%), while playing a smaller role for heterotrophic respiration (30%). In addition, Ahlström et al. (2017) further demonstrated that biases in simulated precipitation, temperature, and downward shortwave radiation can explain up to 40% of the spread in land carbon fluxes and carbon pools estimates among Earth System models. Schaphoff et al. (2006) found that, under future projections, large variations in simulated precipitation patterns can even change the signs of land carbon uptake in tropical and sub-tropical ecosystems.

Global carbon estimates have relied on global atmospheric forcing datasets derived from Earth System models, atmospheric reanalyses, or observation-based products (e.g. Qian et al., 2010; Ahlström et al., 2017; Schaphoff et al., 2006; Morales et al., 2007; Müller et al., 2007; Fisher et al., 2022). Among these datasets, Earth System models and atmospheric reanalyses have typically been provided at coarse spatial resolutions, on the order of 100 km. Even regional estimates have often used coarse atmospheric forcing data, at best around 25 km (Jung et al., 2007a; Vetter et al., 2008; Huntzinger et al., 2013). At such grid spacings, convective processes – one of the two main mechanisms producing precipitation – must be parameterized. Convective parameterizations are known to introduce various biases in the representation of precipitation (e.g. Fiedler et al., 2020). One well-known bias is the overestimation of the frequency of light precipitation events and corresponding underestimation of intense events, commonly referred to as the "drizzle" problem (e.g Sun et al., 2005; Dai, 2006; Lazoglou et al., 2024). Refining the grid spacing to a few kilometers, typically below about 10 km, allows deep convective parameterizations to be switched off and deep convection to be explicitly resolved by the underlying fluid-dynamical equations. Comparisons between km-scale models and coarse-resolution climate models with convective parameterization have consistently shown a reduction of the drizzle problem (e.g. Prein et al., 2015; Schär et al., 2020; Stevens et al., 2020). Instead of drizzling, km-scale models with explicit convection produce more intense and shorter-lived daily precipitation events, in better agreement with observations. This difference in rainfall distribution might project on the carbon cycle. In their offline regional simulation of groundnut yield over West Africa, Garcia-Carreras et al. (2015) showed that the persistent drizzle leads to too high surface evaporation and delays the planting of groundnut by up to 2 months in the south of the simulated domain. In contrast, simulating the short, localized and high-intensity rain events by explicitly resolving convection in the atmospheric forcing leads to an earlier and more realistic triggering of planting.

Here, we propose the hypothesis that explicitly resolved convection enhances gross primary productivity. The underlying idea is that shorter-lived precipitation events allow more radiation to reach the surface on rainy days, thereby increasing photosynthesis and gross primary productivity. To test this hypothesis, we conduct two offline simulations using the terrestrial biosphere model JSBACH (Jena Scheme for Biosphere Atmosphere Coupling in Hamburg) (Schneck et al., 2022). One simulation is performed at a grid spacing of 5 km using atmospheric forcing derived from a 5-km global climate simulation with explicit convection, while the other simulation is conducted at a grid spacing of 160 km with atmospheric forcing taken from a coarse-resolution climate (160 km) model with parameterized convection. To reduce computational costs, particularly those associated with spinning up the carbon pools, we confine our study domain to Europe.

The outline of the paper is as follows: Section 2 describes the JSBACH model and the design of the two experiments. Section 3 first quantifies the carbon fluxes and their differences in the two simulations, focusing on gross primary productivity, autotrophic respiration, heterotrophic respiration and grazing by herbivores. It then explains for each carbon flux the mechanisms underlying the differences found between the two simulations, especially testing the previously mentioned hypothesis. Section 4 summarizes and discusses the results.

2 Model description

2.1 JSBACH

JSBACH version 4 (Schneck et al., 2022) is the land component of the ICON Earth System model and its previous version was the land component of ICON's predecessor, the MPI Earth System model (Mauritsen et al., 2019). JSBACH represents both the physical and the biogeochemical cycle of the land surface. Soil temperature is computed by solving the thermal diffusion equation, discretized over a finite number of soil layers. Soil moisture is predicted by the one-dimensional Richards equation. For the biogeochemical cycle, we only consider the carbon cycle without any disturbance (e.g., fire). The core of the carbon module consists of assimilation of carbon through photosynthesis and the loss of water and carbon through plants transpiration. These processes are parameterized using components of the BETHY model (Knorr, 1997, 2000). The photosynthesis module first computes potential productivity under the assumption of unlimited water availability. Using unstressed stomatal conductance, the potential water loss through transpiration is calculated, from which the water-stressed stomatal conductance is derived. With this actual stomatal conductance, the model then computes the actual productivity per leaf area. The photosynthesis module accounts for physiological differences between plants by using the Farquhar model for C3 plants (Farquhar et al., 1980) and the Collatz model (Collatz et al., 1992) for C4 plants. Gross primary productivity is obtained by multiplying productivity per leaf area by the leaf area index, which is simulated using the phenology model LoGro-P (Logistic Growth Phenology). Net primary productivity is determined by subtracting autotrophic respiration from gross primary productivity. Net primary productivity is then allocated to three carbon pools: the wood pool (stems, branches, and roots), the green pool (leaves, fine roots, and vascular tissues), and the reserve pool (sugars and starches). The green pool looses carbon to the atmosphere through grazing by herbivores. The three carbon pools loose carbon to the soil through litterfall processes such as shedding of leaves, sapwood and littering. The soil carbon module consists of woody and non-woody litter, which can occur above or below ground, each being subdivided into ethanol, acid, water and nonsoluble. There are also two humus pools, one for woody and one for non-woody litter. This makes a total of 18 soil carbon pools. The dynamics of litter and soil carbon are parameterized using the Yasso07 model (Liski et al., 2005; Tuomi et al., 2009). Carbon is returned from the soil to the atmosphere via heterotrophic respiration. Hence, in equilibrium, carbon uptake through gross primary productivity is balanced by carbon losses through autotrophic respiration, heterotrophic respiration and grazing by herbivores.

2.2 Experimental design

We conduct two offline simulations with the JSBACH model, integrated on an icosahedral grid and on a limited domain covering Europe (Fig. 1a and b). The two simulations are integrated at two distinct grid spacings with corresponding distinct atmospheric forcings. For the first simulation, we use atmospheric forcing derived from a global storm-resolving simulation conducted with the Sapphire configuration of the ICON model (Hohenegger et al., 2023) at that same grid spacing of 5 km and on the same grid, modulo its global extent. The set-up of the ICON simulation is described in Segura et al. (2025), where it is referred to as ICON-C3. ICON-C3 also employs JSBACH as a land surface model, but in its light version, simulating only soil temperature and soil moisture and using climatological distribution of vegetation parameters instead of plant functional types. The lack of a simulation with carbon cycle at storm-resolving resolution motivated this study. The atmospheric forcing from ICON-C3 is available every 3 hours. It represents perpetual 2020 conditions. ICON-C3 had been integrated for five years to sample interannual variability. The first year of the five-year ICON-C3 simulation is excluded as spin-up. The second offline JSBACH simulation is integrated at a grid spacing of 160 km and uses atmospheric forcing derived from the MPI-ESM1.2-LR.ssp245 (Wieners et al., 2019) simulation, which was originally provided on the native MPI-ESM1.2-LR atmospheric grid. Before being used by JSBACH, the forcing variables are remapped to the 160-km triangular grid using a distance-weighted average of the four nearest neighbor values. We choose the SSP2.45 scenario and the year 2021 as we do not have perpetual 2020 conditions from a low-resolution model, and that year had the closest atmospheric CO_2 concentration compared to the one used in ICON-C3. MPI-ESM1.2-LR.ssp245 uses the full version of JSBACH, including plant functional type and carbon cycle, but with prescribed atmospheric CO_2 concentration. We nevertheless do not directly use the carbon variables of MPI-ESM1.2-LR.ssp245 for comparison with our offline 5-km simulation to allow for a cleaner comparison, using instead the same land surface model version without atmospheric coupling. The atmospheric forcing of MPI-ESM1.2-LR.ssp245 is available every 6 hours. To sample interannual variability, we conduct six individual simulations, each driven by the atmospheric forcing of the year 2021 taken from the ensemble members r1i1p1f1 to r6i1p1f1. In the following, we refer to the first JSBACH simulation as SRM (for storm-resolving model) and the second one as LR (for low resolution). The atmospheric forcing variables needed to drive JSBACH are surface precipitation, downward shortwave and longwave radiation, as well as the near-surface (lowest atmospheric layer) humidity, temperature and wind speed. In both offline simulations, the atmospheric CO_2 concentration is prescribed at a constant reference value of 367 ppm. First, we use a constant rather than transient value to avoid having to simulate a long period, like several repetitions of a 30 year period, due to the computational cost and to simplify the analysis. Second, we choose a concentration which has often been used to represent "present-day" conditions in idealized studies. Using other CO_2 concentration would change the size of the carbon pools at equilibrium, but not the differences between SRM and LR as those can be fully explained by differences in the atmospheric forcing (see section 3).

To estimate carbon fluxes, JSBACH also needs land parameter maps, such as albedo, soil type and plant functional type. These land parameter maps are derived from corresponding high-resolution observational datasets, with grid spacings of O(1 km) or finer and these maps are coarsened to the targeted grid spacings of 5 km and 160 km. For plant functional type, we use the ESA CCI land cover map (Store, 2019), which provides land cover type at a grid spacing of 300 m. We convert these land cover types to the plant functional types expected by JSBACH using a cross-walking table. In both simulations, we consider the default 11 plant functional types of JSBACH. To ensure a consistent comparison, we restrict the analysis to grid cells with a land fraction of 100% in both simulations.

Both the SRM and LR simulations start from zero carbon fluxes and carbon pools. Thus, it is necessary to spin up the simulations over many years to reach equilibrium values. The humus pools require the longest time to spin up because they are associated with the slowest turnover processes. To accelerate the spin-up, JSBACH provides a special workflow that analytically estimates the equilibrium value of the humus pools based on their transient behavior. The humus pool values are then replaced by this analytically predicted equilibrium value. In the SRM and LR simulations, this workflow is applied once the difference in carbon flux into the humus pools between two consecutive years becomes smaller than 0.001 g C m^{-2} at every grid cell. After this step, the spin-up continues until the absolute difference in total ecosystem carbon between consecutive years is less than 1 g C m^{-2} at every grid cell, following McGuire et al. (1992) and Hoffman et al. (2014). The total spin-up time amounts to 556 years for the SRM simulation and between 468 to 484 years for the LR six simulations. After the carbon pools reach equilibrium, the simulations are continued for an additional four years for the SRM, and the mean over these four years is used for analysis. For each of the LR member, the simulation is continued for one additional year and the mean over the six members is used for analysis.

The SRM simulation is driven by atmospheric forcing coming from a storm-resolving model with an explicit representation of convection, whereas convection was parameterized in the atmospheric forcing driving LR. This allows testing our hypothesis regarding the effect of resolving the short-lived nature of storms on carbon. At the same time, the two forcings were derived from two models that differ more than just by their representation of convection. Even though both models are supposed to represent the year 2021, their simulated climate will not be identical. Moreover, high resolution also comes with a better representation of orgography and land surface properties. All these factors can confound the direct effect of resolving storms and complicate the analysis. We nevertheless retain all these baseline differences in our primary simulations to be able to assess whether the effect of precipitation duration on carbon fluxes is sufficiently strong and systematic to emerge despite these structural differences.

3 Result

3.1 Quantification of carbon flux differences

Figure 1 shows the four components of the carbon budget over the simulation domain (Europe), averaged over time/members, for LR, SRM, and their difference (SRM minus LR). The four components are: Gross Primary Productivity (GPP), autotrophic Respiration (Ra), heterotrophic Respiration (Rh) and grazing by herbivores. Because the simulations are in equilibrium, GPP is on average balanced by respiration and grazing and net ecosystem productivity is zero. Figure 1 reveals that the carbon fluxes are generally smaller in SRM than in LR, especially over central eastern Europe (Belarus, Ukraine, Romania, Moldova, Serbia, Hungary, Slovakia, Czech Republic, Poland, and Turkey). The differences are largest for GPP. Nevertheless, all four carbon fluxes exhibit a similar spatial difference pattern, with strongest negative differences over central eastern Europe and weaker negative, up to slightly positive, differences elsewhere. This difference pattern mostly reflects the spatial pattern of the carbon fluxes in SRM. Whereas the carbon fluxes in LR show very little zonal variations, there is a clear east-west contrast in SRM with smaller values over central eastern Europe.

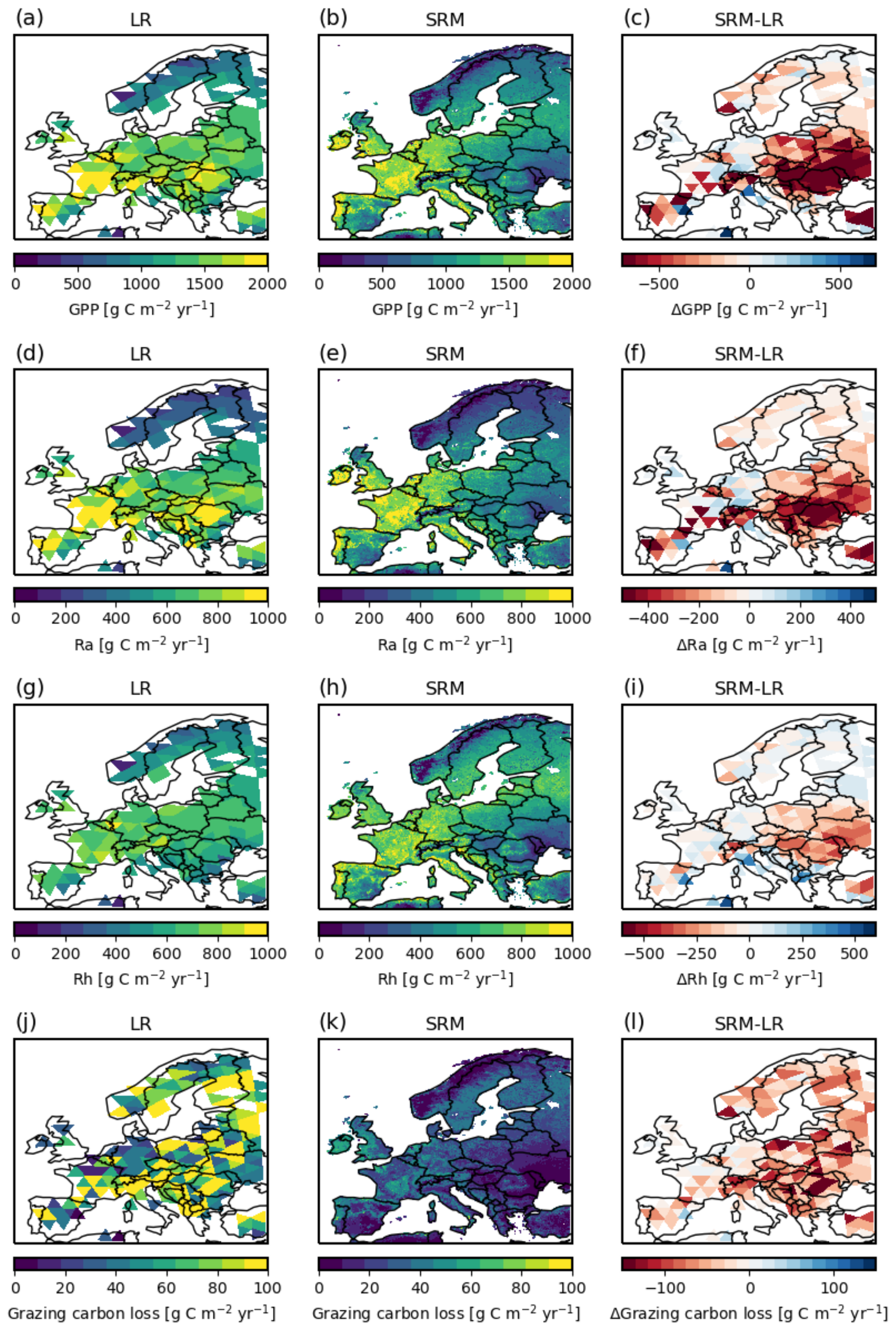

Figure 1. Carbon fluxes averaged over time/members with (a-c) gross primary productivity (GPP), (d-f) autotrophic respiration (Ra), (g-i) heterotrophic respiration (Rh), and (j-l) carbon loss by grazing of herbivores for (left) LR, (center) SRM, and (right) the resulting difference (SRM-LR).

In addition, SRM shows much finer spatial structure in the simulated carbon fluxes than LR (Fig. 1). This difference is expected, as small-scale surface spatial variability is well resolved in the SRM, especially along the Alps, Carpathian, Pyrenees and Scandinavian mountains with the underlying high-resolution topography and land cover type.

To quantify the overall magnitude of the differences in carbon fluxes between the two simulations, we compute the mean carbon fluxes averaged over the land area of the simulation domain (Table 1). On average, SRM exhibits smaller carbon uptake by vegetation than LR. GPP is 1112.5 g C m^{-2} yr^{-1} in SRM, which is 279 g C m^{-2} yr^{-1} less than in LR. Given its smaller carbon uptake, SRM releases less carbon to the atmosphere. Ra reaches 519.2 g C m^{-2} yr^{-1} in SRM, falling below the LR value by 175.7 g C m^{-2} yr^{-1}. In addition, Rh releases less carbon into the atmosphere in the SRM simulation (569.0 g C m^{-2} yr^{-1}) than in the LR simulation (621.2 g C m^{-2} yr^{-1}). The difference in carbon released through grazing by herbivores is -51.2 g C m^{-2} yr^{-1}.

Table 1. Gross primary productivity (GPP), autotrophic respiration (Ra), heterotrophic respiration (Rh) and carbon loss by grazing of herbivores as averaged over Europe (land area of the domain) and time/members (in g C m^{-2} yr^{-1}).

Variables	LR	SRM	Difference (SRM-LR)
GPP	1391.5	1112.5	-279
Ra	694.9	519.2	-175.7
Rh	621.2	569.0	-52.2
Grazing	75.4	24.2	-51.2

To put these numbers into context, estimates of GPP generally show larger values over western central Europe than over eastern Europe and the Iberian Peninsula (e.g., Zhu et al., 2025; Pu et al., 2025; Yuan et al., 2025; Kang et al., 2025; Chen et al., 2024). Although uncertainties in GPP retrievals are large and different datasets do not always agree, values over western central Europe are typically around 1500-2000 g C m^{-2} yr^{-1}. The observed spatial pattern and averaged values are qualitatively consistent with the results shown in Fig. 1a and b. For Ra, the simulated values shown in Fig.1d and e also broadly agree with observation estimates, which typically range between 1000-1500 g C m^{-2} yr^{-1} over western central Europe (Ai et al., 2018; Zhu et al., 2025; Yuan et al., 2025). Regarding heterotrophic respiration, the dataset presented in Tang et al. (2020) has values of around 400-600 g C m^{-2} yr^{-1} in humid temperate areas over western and central Europe. These values are lower than those reported by Hashimoto et al. (2015), which range between 750-1000 g C m^{-2} yr^{-1} over western central Europe. The JSBACH simulations shown in Fig. 1g and h are thus in better agreement with the estimate reported by Hashimoto et al. (2015). The domain-mean GPP for Fluxnet2015 tower measurements (Pastorello et al., 2020) is 1480.6 $\pm$ 523.3 g C m^{-2} yr^{-1} (standard deviation across towers). In comparison, the gridded MODIS/Terra dataset (Running and Zhao, 2021) yields a lower domain-mean of 1123.6 g C m^{-2} yr^{-1}. While the Multi-scale Synthesis and Terrestrial Model Intercomparison Project (MsTMIP) simulations (Huntzinger et al., 2018) show 899.9 $\pm$ 190.8 g C m^{-2} yr^{-1} (standard deviation across model members). In MsTMIP, Ra and Rh are estimated at 475.7 $\pm$ 154.8 and 447.1 $\pm$ 171.9 g C m^{-2} yr^{-1}, respectively. Overall, the JSBACH simulations (Table 1) reproduce the reported carbon flux magnitudes reasonably well. However, it should be noted that the use of steady-state and not transient historical forcing for our offline simulations makes a one-to-one comparison to observations difficult. Our comparison with Fluxnet2015, MODIS, and MsTMIP is intended solely to verify that the simulated carbon fluxes fall within a broadly realistic and biologically sound parameter space, rather than to serve as a strict validation.

3.2 What causes the differences in carbon fluxes?

3.2.1 Gross primary productivity

To first order, photosynthesis is mainly controlled by the amount of solar radiation, temperature and water availability (soil moisture) (Nemani et al., 2003; Beer et al., 2010). This is also the case in JSBACH, where GPP is modeled as a function of leaf area index and water-stressed plant productivity. For vegetation across Europe, leaf area index is mainly controlled by temperature and soil moisture, whereas plant productivity depends in particular on solar radiation and soil moisture. Table 2 shows the results of a multiple linear regression of GPP against surface downward shortwave radiation (SW), air temperature ($\mathrm{T_a}$), and root-zone soil moisture. In both SRM and LR, downward shortwave radiation plays the dominant role among the three factors. In both simulations, the regression coefficient for downward shortwave radiation is larger than 0.57, whereas the other two regression coefficients are smaller than 0.21.

Table 2. Coefficients from the multiple linear regression of GPP with respect to downward solar radiation (SW), air temperature ($\mathrm{T_a}$) and root-zone soil moisture (SM), $\mathrm{GPP} = \beta_0 + \beta_{\mathrm{SW}} \cdot \mathrm{SW} + \beta_{\mathrm{T_a}} \cdot \mathrm{T_a} + \beta_{\mathrm{SM}} \cdot \mathrm{SM}$. Each dependent and independent variable is standardized to have zero mean and unit variance. Daily values at every grid point are used to compute the multiple linear regression.

Simulations	β_0	β_{SW}	$\beta_{\mathrm{T_a}}$	β_{SM}
LR	0	**0.60**	0.18	0.19
SRM	0	**0.57**	0.10	0.21

The regression analysis confirms the idea underlying this work mentioned in the introduction, namely that the shift in the convective precipitation distribution – from long-lived drizzling rainfall in models with convective parameterization to short-lived storms in models with explicit convection – could affect GPP via change in cloud cover and radiation. Yet, the documented changes in GPP in section 3.1 are opposed to the expectations. GPP is decreased, not increased in SRM compared to LR. To understand this apparent contradiction, we examine in more detail the relationships between GPP, precipitation, radiation, and precipitation duration (see Fig. 2).

Figure 2a reveals that GPP steadily decreases in LR as rain intensifies beyond about 10 mm day^{-1}, whereas it stays constant in SRM. This behavior is consistent with the relationship between precipitation and downward shortwave radiation (Fig. 2b). In LR, radiation starts to decrease rapidly beyond 9 mm day^{-1} of precipitation, while it stays approximately constant with increasing precipitation in SRM. The fact that SRM can maintain higher solar radiation than LR by same precipitation amount could be due to shorter-lived precipitation events, as confirmed by Fig. 2c. Although SRM has slightly more rainfall events lasting 6 h and 12 h, it has substantially fewer full-day rainy days than LR. Rain occurring throughout the entire day accounts for only 17.6% in SRM, compared to 45.1% in LR.

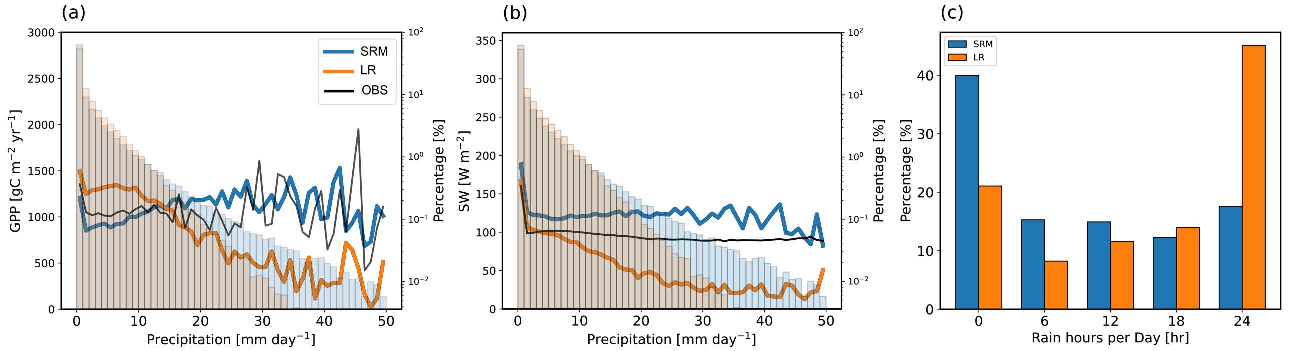

Figure 2. (a) Daily mean GPP as a function of daily mean precipitation for LR (orange line) and SRM (blue line) together with their histogram of precipitation (bar). Black line for observations, taken from the Fluxnet dataset and retaining one year of observations per station with at least one full year of non-missing values between 2018-2022 (118 stations). (b) Same as (a) but for surface downward shortwave radiation. Observations are taken from the gridded E-OBS dataset and averaged over the years 2018-2022. (c) Histogram of rain hours per day in the two simulations.

To further confirm that the distinct relationship between GPP and precipitation between LR and SRM as precipitation strongly intensifies is due to shortwave radiation and not to other confounded co-varying climate factors, we conducted a sensitivity experiment where we replaced the shortwave radiation forcing in LR by the one from SRM (Fig. S1). This removes the previously observed decline in GPP with precipitation. As for this sensitivity experiment the 3-hourly SRM forcing was aggregated to a 6-hourly forcing to be consistent with the LR forcing, we can further conclude that the difference in forcing frequency is also not the reason for the distinct behavior between LR and SRM. Note that, although switching the radiation forcing in LR removes the decline in GPP as precipitation intensifies, the values remain much larger in LR than in SRM for a given precipitation amount. This pinpoints to an effect of the simulated mean climate on GPP, an effect discussed further below.

Our analysis isolates the distinct behavior of downward surface shortwave radiation between LR and SRM to be the root cause for the decline in GPP with intensifying precipitation in LR, a distinct behavior that we hypothesize as being due to the representation of convection. If this is true, we would expect the decline in GPP with strongly intensifying precipitation in LR to be more pronounced during the summer season, at a time of peak convective activity. Only during summer, the convection scheme in LR produces more than half of the mean precipitation. The contribution is 56% in JJA, versus 31%, 23% and 12% in MAM, SON and DJF, respectively. Plotting the GPP-precipitation relationship as a function of season (Fig. S2) confirms that the GPP decline in LR is only visible during the summer season. Moreover, the GPP decline in LR should also be relatively independent of the underlying plant functional type, as further confirmed by Fig. S3. There, the differences between SRM and LR are smallest for grassland, which occupies 23.91% and 23.87% of the land points of the domain in LR and SRM, respectively. As such and if anything, the larger fraction of grassland in LR should have made the domain-mean GPP curve more akin to the SRM one; slight differences in the fractions of plant functional types between SRM and LR can also not explain the distinct behavior of GPP with intensifying precipitation between the two models.

The strong decline in GPP with precipitation in LR leads to smaller GPP values in LR compared to SRM beyond a precipitation threshold of about 14 mm day^{-1}. To quantify the impact of these strong precipitation events on the overall mean GPP, we decompose the mean GPP into contributions from days with less than and greater than 14 mm day^{-1} of precipitation:

$$\overline{\mathrm{GPP}} = \alpha \cdot \overline{\mathrm{GPP}_{\mathrm{P}<14}} + (1-\alpha) \cdot \overline{\mathrm{GPP}_{\mathrm{P}\geq 14}}, \quad (1)$$

where the overbar denotes averaging, P is precipitation and α is the fraction of events with $\mathrm{P} < 14$ mm day^{-1}. The values of each term are summarized in Table 3.

Table 3. Decomposition of land mean GPP (g C m^{-2} yr^{-1}) based on a daily mean precipitation threshold of 14 mm day^{-1} (see Eq. 1.)

Simulation	$\overline{\mathrm{GPP}}$	$\alpha \cdot \overline{\mathrm{GPP}_{\mathrm{P}<14}}$	$(1-\alpha) \cdot \overline{\mathrm{GPP}_{\mathrm{P}\geq 14}}$	α	$\overline{\mathrm{GPP}_{\mathrm{P}<14}}$	$\overline{\mathrm{GPP}_{\mathrm{P}\geq 14}}$
LR	1391.5	1391.4	0.1	0.9998	1391.7	457.3
SRM	1112.5	1073.3	39.1	0.97	1110.9	1159.7
SRM-LR	-279	-318.1	39	-0.0298	-280.8	702.4

Table 3 shows that the contribution is larger in SRM than in LR for the strong precipitation events ($(1-\alpha) \cdot \overline{\mathrm{GPP}_{\mathrm{P}\geq 14}}$), whereas it is smaller for weak precipitation events ($\alpha \cdot \overline{\mathrm{GPP}_{\mathrm{P}<14}}$). The larger GPP under strong precipitation events in SRM can nevertheless not overcompensate for the weaker GPP values below the precipitation threshold of 14 mm day^{-1}. In other words, the smaller GPP on weakly precipitating days explains the smaller domain-mean GPP in SRM. The larger contribution of strong precipitation days to GPP in SRM than in LR, $(1-\alpha) \cdot \overline{\mathrm{GPP}_{\mathrm{P}\geq 14}}$, arises both from the larger conditional average of GPP, $\overline{\mathrm{GPP}_{\mathrm{P}\geq 14}}$, consistent with Fig. 2b, and from the more frequent occurrence of strong precipitation events, which is expected when convection is explicitly resolved.

Why is GPP in general smaller in SRM than in LR, and especially so in central eastern Europe (Fig. 1)? The sensitivity experiment in Fig. S2 with using the shortwave radiation forcing of SRM in LR already indicated that the smaller GPP in SRM cannot be due to shortwave radiation, as using this forcing actually further enhances GPP in LR. Conducting two new sensitivity experiments (see Fig. S2), also replacing the precipitation forcing (red curve), as well as the temperature forcing (green curve) in LR with the SRM forcing, brings the GPP curve in LR down close to the SRM one. Replacing precipitation leads to a reduction in GPP of 28.6 g C m^{-2} yr^{-1}, whereas replacing temperature leads to an additional reduction of 14.3 g C m^{-2} yr^{-1}. Hence, differences in the precipitation forcing between SRM and LR are the main reason for the weakening of GPP in SRM. Figure 3a shows the corresponding mean precipitation distribution, revealing widespread smaller precipitation values in SRM. GPP does not directly depend upon precipitation, but on soil moisture, both through the controls of soil moisture on leaf area index and on photosynthesis. Figure 3b shows the the corresponding soil moisture difference. The averaged difference pattern in soil moisture resembles that of GPP in Fig. 1c, particularly the strong negative values over central eastern Europe. In conclusion, the smaller precipitation values in the SRM forcing leads to more water stress for the plants and ultimately smaller

GPP, masking the effect of enhanced radiation due to shorter-lived storms. The importance of precipitation and soil moisture for GPP has been documented in past studies (e.g. Beer et al., 2010; Humphrey et al., 2021). Our findings are also consistent with the result of the multiple linear regression shown in Table 2, where soil moisture appears to play an important role for GPP.

Our analysis reveals two key differences between LR and SRM, which act in an opposite way on GPP: More radiation in SRM due to shorter-lived precipitation events, favorable for photosynthesis, but drier climate, enhancing limitiation of productivity due to water stress. As these characteristics are related to the distinct atmospheric forcing of the two models, one may wonder which characteristic is closer to observations. We compare the forcings to observations from the E-OBS dataset, which is a gridded dataset from station observations over Europe (Cornes et al., 2018). We select the years 2018-2022 in E-OBS to stay close to the simulated year but account for some interannual variability, and regrid the dataset to the LR grid spacing. In terms of annual mean temperature or precipitation distribution, the performance in LR and SRM is similar. Domain-mean differences over land points are -0.6 K in LR versus -1 K in SRM for temperature and 0.24 mm day^{-1} in LR versus 0.46 mm day^{-1} in SRM for precipitation. The smaller mean error in LR is a result of a better compensation between positive and negative biases in LR. In absolute values, the biases are actually smaller over 60% of the land points of the domain in SRM compared to LR. During the summer season though, precipitation is too weak over central eastern Europe in SRM compared to E-OBS, indicating that the GPP values may be too small there. In contrast, the relationship between shortwave radiation and precipitation (see black curve in Fig. 2b) is better captured in SRM than in LR. Also in observations, shortwave radiation does not decline as steeply as in LR with intensifying precipitation, with a decline of about 7 W m^{-2} between 10 and 20 mm day^{-1} of precipitation, versus 50 W m^{-2} in LR. It nevertheless seems that SRM simulates too much solar radiation. In terms of GPP, also in the FLUXNET observations (see black curve in Fig. 2a), GPP does not exhibit a strong decrease with intensifying precipitation, making this characteristic more akin to the SRM results (see also discussion section). The very good agreement between the observational and the SRM curve in Fig. 2a has to be taken with some caution as there might be compensating errors in SRM with too high solar radiation and potentially too weak mean precipitation. Furthermore, despite the use of 116 stations, the stations are not evenly distributed throughout the simulated domain.

3.2.2 Autotrophic respiration

In JSBACH, Ra consists of dark respiration (maintenance respiration) and growth respiration. Dark respiration per leaf area is a function of air temperature and downward shortwave radiation, following the Farquhar and Collatz models of photosynthesis, whereas growth respiration is proportional to GPP. Table 4 shows the result of the multiple linear regression between Ra and its controlling factors, namely GPP, T_a and SW. It is clear from Table 4 that GPP is the dominant controlling factor with a regression coefficient of 0.86 in both simulations. Further examining the relationship between GPP and Ra using Fig. 4, we see that Ra indeed increases linearly with GPP in both simulations over the range of simulated GPP values. The functional relationship is identical in both simulations up to a GPP value of about 2500 g C m^{-2} yr^{-1}. Because LR produces a larger mean GPP, and also simulates more frequent GPP values larger than 2500 g C m^{-2} yr^{-1} whose associated Ra values are larger

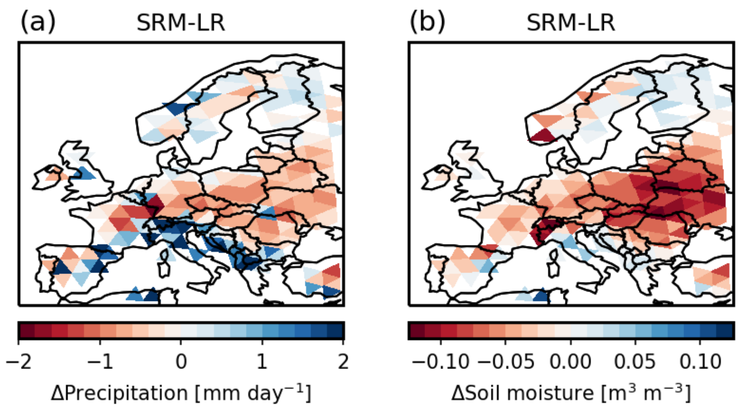

Figure 3. Maps of difference in (a) precipitation (mm day^{-1}) and (b) soil moisture (first soil layer) (m^3 m^{-3}) between SRM and LR averaged over the simulated years and members.

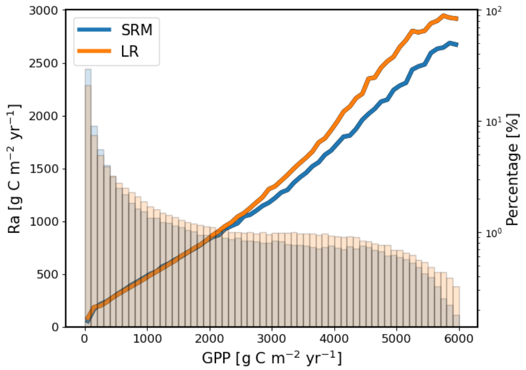

Figure 4. Daily mean values of Ra as a function of daily mean values of GPP for the LR (orange line) and the SRM (blue line) simulations with histogram of GPP (bar).

in LR than in SRM, Ra is also larger on average in LR than in SRM. The mean value is 694.9 g C m^{-2} yr^{-1} in LR, which is 175.7 g C m^{-2} yr^{-1} larger than in SRM.

Table 4. Same as Table 2 but from the multiple linear regression of Ra with respect to GPP, T_a and SW, $Ra = \beta_0 + \beta_{GPP} \cdot GPP + \beta_{T_a} \cdot T_a + \beta_{SW} \cdot SW$.

Simulations	β_0	β_{GPP}	β_{T_a}	β_{SW}
LR	0	**0.86**	0.14	-0.065
SRM	0	**0.86**	0.20	-0.088

3.2.3 Heterotrophic respiration

Rh is modelled using the Yasso07 scheme (Liski et al., 2005; Tuomi et al., 2009). It is proportional to soil carbon pool size, pool specific decomposition rates and a climate-dependent pool-independent parameter k_{clim}. The latter is given as

$$k_{\mathrm{clim}} = e^{\beta_1 \overline{\mathrm{T_c}} + \beta_2 \overline{\mathrm{T_c}}^2}(1 - e^{\gamma \overline{\mathrm{P_m}}}), \tag{2}$$

where $\overline{\mathrm{T_c}}$ is the 30-day mean air temperature in °C and $\overline{\mathrm{P_m}}$ is the 30-day mean precipitation in m yr^{-1}. The parameters β_1=0.095 °C^{-1}, β_2=-0.0014 °C^{-2}, and γ=-1.21 yr m^{-1} are fitted parameters. The k_{clim} plays an equivalent role to the Q10 parameter in other soil carbon models. Through k_{clim}, Rh is a function of monthly mean air temperature ($\overline{\mathrm{T_a}}$) and precipitation ($\overline{\mathrm{P}}$) simulated by the LR and SRM forcing datasets. The formulation therefore responds to monthly-scale precipitation amount but does not distinguish rainfall-event frequency, intensity, or duration when $\overline{\mathrm{P}}$ is unchanged. The analysis below therefore concerns differences in monthly-scale precipitation climatology between SRM and LR, rather than the short-duration versus persistent-rainfall mechanism examined for GPP in Sect. 3.2.1.

We first examine the impact of potential differences in k_{clim} on Rh, before discussing the potential influence of differences in pool sizes. We start with the analytic solution of k_{clim} from Eq. (2) to understand the influence of $\overline{\mathrm{T_a}}$ and $\overline{\mathrm{P}}$ on k_{clim} (see the grey contour lines in Fig. 5). When $\overline{\mathrm{P}}$ <4 mm day^{-1}, k_{clim} increases with both temperature and precipitation, reflecting the fact that decomposition becomes more active under moist and warm conditions. When $\overline{\mathrm{P}} \geq$ 4 mm day^{-1}, k_{clim} becomes largely insensitive to further increases in precipitation and instead increases mainly with temperature. This weak sensitivity to precipitation suggests that moisture is no longer a limiting factor for decomposition, because moisture is already large enough in $\overline{\mathrm{P}}$ ≥4 mm day^{-1} conditions.

Using the insight from the analytic solution of k_{clim}, we investigate why Rh could be smaller in SRM (569.0 g C m^{-2} yr^{-1}) than in LR (621.2 g C m^{-2} yr^{-1}). Looking at Fig. 5a and b, we see that most data points in both simulations occur under $\overline{\mathrm{P}}$ <4 mm day^{-1} condition (≥92%), where both precipitation and temperature influence k_{clim}. A visual comparison of these two panels suggests that SRM contains more data points at smaller monthly mean precipitation amounts than LR. This is confirmed by Fig. 5c, especially in the precipitation histogram on the right. SRM has more data points than LR when $\overline{\mathrm{P}}$ ≤1.5 mm day^{-1}, by 8%, corresponding to a frequency of occurrence of 37%. In contrast, LR has more data points when 1.5< $\overline{\mathrm{P}}$ ≤4 mm day^{-1}, by 10%, and its frequency of occurrence is 59%. A larger occurrence of smaller monthly mean precipitation amounts implies a smaller k_{clim}, which is consistent with the weaker Rh found in SRM compared to LR. Likewise, the median value of $\overline{\mathrm{P}}$ is smaller in SRM compared to LR, with a value of 1.9 versus 2.2 mm day^{-1}, respectively.

Looking now at the temperature dependency, SRM has more data points for 271< $\overline{\mathrm{T_a}}$ <278 K and $\overline{\mathrm{T_a}}$ >292 K, whereas LR has more data points for 278<$\overline{\mathrm{T_a}}$ <292 (see particularly the temperature histogram in Fig. 5c). The medians of $\overline{\mathrm{T_a}}$ are 281 K in SRM and 281.8 K in LR, hence the median is colder in SRM. This effect would suggest a smaller k_{clim} and therefore smaller Rh in SRM compared to LR, acting in the similar direction as precipitation. If only $\overline{\mathrm{P}}$ decreases from the median LR value (2.2 mm day^{-1}) to the SRM value (1.9 mm day^{-1}), k_{clim} would decrease by 0.110. If only $\overline{\mathrm{T_a}}$ decreases from the median LR value (281.8 K) to the SRM one (281 K), k_{clim} would decrease by 0.071. The effect of precipitation, therefore, dominates. This is also consistent with the findings of Tang et al. (2020), who used a random forest algorithm to derive a gridded Rh dataset

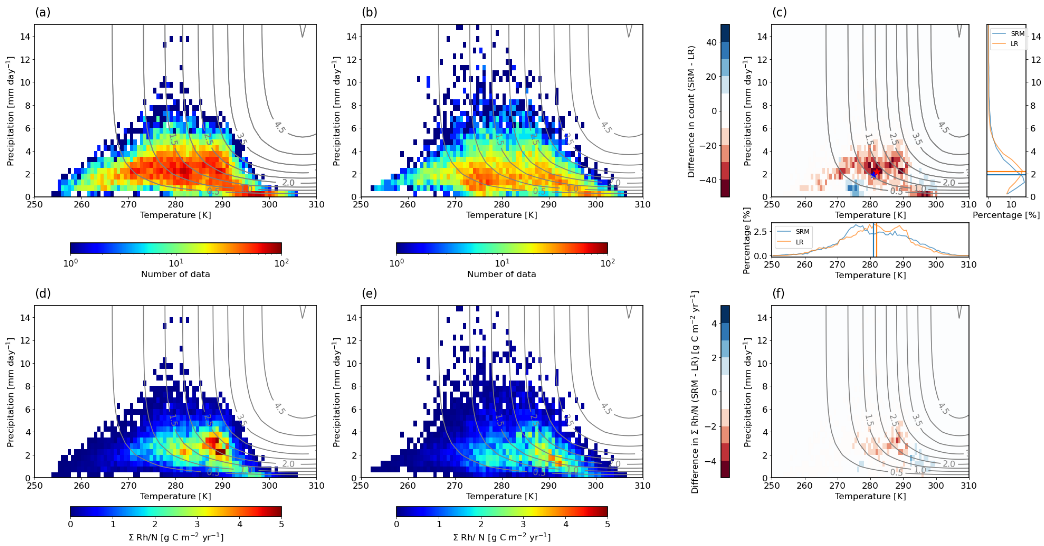

Figure 5. (a, b) Two-dimensional histogram (shading) of monthly mean air temperature and precipitation in (a) the LR simulation, (b) the SRM simulation and (c) their difference (SRM-LR). In panel c, the two insets are for the histogram of precipitation (right) and of temperature (bottom). Stars indicate medians of monthly mean air temperature and precipitation in the LR simulation (red star) and in the SRM simulation (blue star). The lower row (d-f) shows the contribution of each bin to the mean of Rh, which is computed as the sum of Rh within each bin divided by the total number of data for (d) the LR simulation, (e) the SRM simulation and (f) their difference, see text for more detail. Grey contour lines represent the analytic solution of k_{clim}, see Eq. 2.

based on field observations from the Global Soil Respiration Database and environmental drivers. According to their study, precipitation is the main driver for Rh for latitudes between 25° and 50°N, whereas temperature becomes the dominant driving factor north of 50°N. Using the dataset produced by Hashimoto et al. (2015), which was based on a semi-empirical model, they even found precipitation and soil moisture to be the dominant drivers across Europe.

The above interpretation relies on k_{clim} as a proxy for Rh rather than directly on the values of Rh. In Fig. 5d-f, we now plot the values of Rh as a function of $\overline{\mathrm{T_a}}$ and $\overline{\mathrm{P}}$. To do so, we first sum all the values of Rh within each bin ($\sum \mathrm{Rh}$) and then divide this sum by the total number of data points (N=8,736), yielding $\sum \mathrm{Rh}/N$ for each bin. If we sum $\sum \mathrm{Rh}/N$ over all bins, we get the value of Rh listed in Table 1. Figures 5d-f indeed show that LR contributes more strongly to Rh than SRM where the values of k_{clim} are also higher, for example around 290 K and 2 mm day^{-1}. Near $k_{\mathrm{clim}} = 2$, $\sum \mathrm{Rh}/N$ peaks in LR, with values exceeding 5 g C m^{-2} yr^{-1}. In contrast, near $k_{\mathrm{clim}} = 1.5$, $\sum \mathrm{Rh}/N$ peaks in SRM, with values of about 3.5 g C m^{-2} yr^{-1}.

Figures 5d and e show that variations in Rh do not perfectly follow k_{clim}. This is a result of the further dependency of Rh on soil carbon pool size. Changing pool sizes, especially if the carbon pools would be smaller in SRM compared to LR, could be the main reason for the differences in Rh, rather than climate effects. The three pools in JSBACH (see section 2.1) are woody litter, non-woody litter and humus. Each of these pools has pool specific decomposition rates. Woody and non-woody litter are sub-divided into ethanol, acid, water and non-soluble, each with their own decomposition rates. The key difference between the woody and the non-woody litter pool is that the decomposition rates in woody litter are multiplied by a factor that represent the pore size, about 0.53.

The humus pool is always larger in SRM than LR, in mean by 3.8 Pg C. In contrast, the litter pool is always smaller in SRM than LR, by 3.3 Pg C. Even though as net effect the total soil carbon pool is larger in SRM than in LR, since the decomposition rate of the humus pool is at least a factor 10 smaller than the ones of the litter pool, the different pool sizes between SRM and LR could still lead to an overall reduction of Rh, depending on how the woody and non-woody litter changes. We compute the subdivision of the litter pool in its two components only once per month and only for one year/one member of the SRM and LR simulation sets as this computation requires writing out all the carbon pools on all plant functional types for every grid point and adds 220 variables to the output. As the pool sizes do not exhibit large temporal variations, this seems sufficient. The non-woody litter is again slightly larger in SRM, with a mean value of 29.4 Pg C versus 29.2 Pg C in LR, whereas the woody litter is smaller in SRM, with a value of 10.6 Pg C versus 13.3 Pg C in LR. The smaller woody litter pool in SRM explains the smaller litter pool in SRM, but the decomposition rates of the woody litter pool are only half the values of the ones of the non-woody litter pool and the pool size is also only about half the non-woody one. Factoring in the pool specific decomposition rates, but neglecting any potential change in k_{clim} by setting it to 1, it turns out that the overall respiration should be larger in SRM due to the larger humus and larger non-woody litter pools. Hence, we conclude that the smaller respiration in SRM is primarily due to climate effects.

3.2.4 Grazing of herbivores

Carbon losses due to grazing of herbivores is smaller in SRM, with a value of 24.2 g C m^{-2} yr^{-1} compared to 75.4 g C m^{-2} yr^{-1} in LR. In JSBACH, grazing of herbivores is proportional to the amount of carbon available in the green pool, which represents the carbon stored in the living parts of plants, the "green" part. The green pool is smaller in SRM than in LR by 218.3 g C m^{-2}, as expected from smaller GPP.

4 Summary and discussion

In this study, we investigated the magnitude of the carbon fluxes over Europe in two offline simulations conducted with the land surface model JSBACH. One simulation is driven by atmospheric forcing from a coarse-resolution climate model simulation, referred to as LR, while the other simulation uses atmospheric forcing from a km-scale simulation, referred to as SRM. The coarse-resolution climate simulation had been performed with MPI-ESM1.2-LR.ssp245 at a grid spacing of 160 km, whereas the km-scale simulation had been performed with the Sapphire configuration of the ICON model at a grid spacing of 5 km (ICON-C3). The selected years of the two climate models represent a present day (2021) climate. The key difference between the two climate simulations is that convection is parameterized at 160 km, but explicitly resolved at 5 km. The hypothesis motivating this study is that explicitly resolving convection at the km scale, rather than parameterizing it, leads to shorter and more intense daily precipitation events. Shorter precipitation events imply less longer-lasting cloud cover, hence more shortwave radiation to reach the surface, which can be used by plants for photosynthesis and may enhance gross primary productivity. The two offline simulations were set out to test this hypothesis.

Comparing the two simulations, we find that gross primary productivity is 1112.5 g C m^{-2} yr^{-1} in SRM versus 1391.5 g C m^{-2} yr^{-1} in LR. Regarding carbon losses, autotrophic respiration is smaller in SRM by 175.7 g C m^{-2} yr^{-1} and heterotrophic respiration is also smaller by 52.2 g C m^{-2} yr^{-1}. As SRM exhibits smaller GPP than LR, this a priori contradicts our hypothesis.

To understand the causes of these differences in carbon fluxes, we explored the underlying main driving factors of the carbon fluxes. For gross primary productivity, we find that, beyond a threshold of about 10 mm day^{-1}, gross primary productivity declines with intensifying precipitation in LR, whereas it stays constant in SRM. These events are also associated with larger downward shortwave radiation in SRM and appear to be shorter-lived. For instance, whole day events occur 18% of the time in SRM compared to 45% in LR. In agreement with this diagnostic, using the SRM radiation as forcing in LR removes the decline in gross primary productivity. This confirms our hypothesis that stronger precipitation events are shorter-lived in SRM, allowing more solar radiation to be absorbed by the plants and leading to a higher gross primary productivity.

At the same time, and even though the two forcing datasets aim to represent the same climate, their climate differs. In particular, smaller precipitation values in SRM lead to reduced soil moisture, enhanced water stress and smaller productivity. This effect is especially visible during the summer season over central eastern Europe and is also consistent with the spatial pattern of the carbon fluxes. Carbon fluxes in SRM exhibit a much more pronounced zonal gradient than LR, with weaker values over central eastern Europe, resulting in more pronounced differences to LR over that latter region. Hence, although explicitly resolving convection favors higher gross primary productivity through shorter-lived, intense daily precipitation events, the overall climatology modulates this effect. In our case, the latter effect wins.

Concerning the remaining carbon fluxes, as autotrophic respiration is largely controlled by gross primary productivity, the smaller productivity directly explains the smaller autotrophic respiration found in SRM. Regarding heterotrophic respiration, the more frequent occurrence of drier (in terms of precipitation) monthly mean conditions is the main contributor to the decline in respiration, with a secondary additional contribution from colder monthly mean temperatures in SRM.

The formulated hypothesis, that shorter-lived events when explicitly resolving convection could enhance gross primary productivity is physically sound and should not depend on the particular model used. It has been well-established that convective parameterizations underestimate strong precipitation events and instead produce too long-lasting weak events. One potential caveat though is that JSBACH, as many other land surface models (Zhang et al., 2020), does not distinguish between diffuse and direct radiation. The atmospheric radiative forcing entails the sum of both components, but the distinct effect of direct and diffuse radiation on gross primary productivity is not taken into account in JSBACH. Increase in diffuse radiation can enhance photosynthesis (Gu et al., 2003), even by same radiation amount, and could compensate for the decline in direct shortwave radiation due to enhanced cloudiness. As in our case the total radiative forcing is smaller in LR than in SRM, this would even require that the better light use efficiency of diffuse radiation more than compensate for the smaller total radiative forcing. It is also unlikely that low-resolution models will have the correct fraction of diffuse to direct radiation given that they simulate the wrong distribution of precipitation event durations (Chakraborty and Lee, 2021). Fluxnet observations over Europe do not show a strong decline in gross primary productivity with precipitation, in better agreement with the SRM results, but it remains unclear how much a correct timing or the different light use efficiency of diffuse and direct radiation is important for this.

In contrast, whether gross primary productivity should increase or decrease in mean when resolving storms strongly depends on the simulated mean climate and hence on the specific model biases. The obtained overall decrease in gross primary productivity in SRM may thus not generalize. In our set-up, the lack of precipitation in SRM was not only the main contributor to the decrease in gross primary productivity, but it also contributed to the decreased heterotrophic respiration. JSBACH may be particularly sensitive to this aspect as the Yasso07 soil carbon scheme assumes a direct dependence of soil respiration on precipitation. Other models tend to assume that the moisture control on decomposition acts as a function of soil moisture. Although soil moisture does not only depend on precipitation, the lack of precipitation readily imprinted itself on soil moisture in our case, so that using soil moisture instead of precipitation might not end up making such a big difference. All in all, given that explicitly resolving storms changes the distribution of precipitation, and with it the dependency of shortwave radiation on precipitation via clouds, our study raises the question of the importance of such effects for plant productivity and carbon fluxes. It provides first evidence that this effect in isolation enhances GPP under strong precipitation events.

Author contributions. JL and CH designed research; performed research; analyzed the data; and drafted the paper.

Competing interests. The authors declare no competing interest.

Acknowledgements. The study was supported by the NextGEMS (Grant No. 101003470) and the Max Planck society for the advancement of science. Open access funding is provided by the Max Planck Society. We thank Seung Hee Seo for thorough discussions on the research and writing and Tamara Emmerichs for internally reviewing the manuscript, which helped strengthen and clarify our manuscript. The simulations were performed using the facilities of the DKRZ (Deutsches Klimarechenzentrum).

References

Ahlström, A., Schurgers, G., and Smith, B.: The large influence of climate model bias on terrestrial carbon cycle simulations, Environmental Research Letters, 12, 014 004, 2017.

Ai, J., Jia, G., Epstein, H. E., Wang, H., Zhang, A., and Hu, Y.: MODIS-Based Estimates of Global Terrestrial Ecosystem Respiration, Journal of Geophysical Research: Biogeosciences, 123, 326–352, https://doi.org/https://doi.org/10.1002/2017JG004107, 2018.

Beer, C., Reichstein, M., Tomelleri, E., Ciais, P., Jung, M., Carvalhais, N., Rödenbeck, C., Arain, M. A., Baldocchi, D., Bonan, G. B., Bondeau, A., Cescatti, A., Lasslop, G., Lindroth, A., Lomas, M., Luyssaert, S., Margolis, H., Oleson, K. W., Roupsard, O., Veenendaal, E., Viovy, N., Williams, C., Woodward, F. I., and Papale, D.: Terrestrial Gross Carbon Dioxide Uptake: Global Distribution and Covariation with Climate, Science, 329, 834–838, https://doi.org/10.1126/science.1184984, 2010.

Chakraborty, T. and Lee, X.: Large differences in diffuse solar radiation among current-generation reanalysis and satellite-derived products, J. Climate, 34, 6635–6650, 2021.

Chen, X., Chen, T., Li, X., Chai, Y., Zhou, S., Guo, R., and Dai, J.: A 2001–2022 global gross primary productivity dataset using an ensemble model based on the random forest method, Biogeosciences, 21, 4285–4300, https://doi.org/10.5194/bg-21-4285-2024, 2024.

Collatz, G. J., Ribas-Carbo, M., and Berry, J. A.: Coupled photosynthesis-stomatal conductance model for leaves of C4 plants, Functional Plant Biology, 19, 519–538, 1992.

Cornes, R. C., Van Der Schrier, G., Van Den Besselaar, E. J., and Jones, P. D.: An ensemble version of the E-OBS temperature and precipitation data sets, Journal of Geophysical Research: Atmospheres, 123, 9391–9409, 2018.

Dai, A.: Precipitation characteristics in eighteen coupled climate models, Journal of climate, 19, 4605–4630, 2006.

Farquhar, G. D., von Caemmerer, S. v., and Berry, J. A.: A biochemical model of photosynthetic CO 2 assimilation in leaves of C 3 species, planta, 149, 78–90, 1980.

Fiedler, S., Crueger, T., D'Agostino, R., Peters, K., Becker, T., Leutwyler, D., Paccini, L., Burdanowitz, J., Buehler, S. A., Cortes, A. U., Dauhut, T., Dommenget, D., Fraedrich, K., Jungandreas, L., Maher, N., Naumann, A. K., Rugenstein, M., Sakradzija, M., Schmidt, H., Sielmann, F., Stephan, C., Timmreck, C., Zhu, X., and Stevens, B.: Simulated Tropical Precipitation Assessed across Three Major Phases of the Coupled Model Intercomparison Project (CMIP), Monthly Weather Review, 148, 3653 – 3680, https://doi.org/10.1175/MWR-D-19-0404.1, 2020.

Fisher, J. B., Sikka, M., Block, G. L., Schwalm, C. R., Parazoo, N. C., Kolus, H. R., Sok, M., Wang, A., Gagne-Landmann, A., Lawal, S., et al.: The terrestrial biosphere model farm, Journal of advances in modeling earth systems, 14, e2021MS002 676, 2022.

Friedlingstein, P., O'Sullivan, M., Jones, M. W., Andrew, R. M., Bakker, D. C. E., Hauck, J., Landschützer, P., Le Quéré, C., Luijkx, I. T., Peters, G. P., Peters, W., Pongratz, J., Schwingshackl, C., Sitch, S., Canadell, J. G., Ciais, P., Jackson, R. B., Alin, S. R., Anthoni, P., Barbero, L., Bates, N. R., Becker, M., Bellouin, N., Decharme, B., Bopp, L., Brasika, I. B. M., Cadule, P., Chamberlain, M. A., Chandra, N., Chau, T.-T.-T., Chevallier, F., Chini, L. P., Cronin, M., Dou, X., Enyo, K., Evans, W., Falk, S., Feely, R. A., Feng, L., Ford, D. J., Gasser, T., Ghattas, J., Gkritzalis, T., Grassi, G., Gregor, L., Gruber, N., Gürses, O., Harris, I., Hefner, M., Heinke, J., Houghton, R. A., Hurtt, G. C., Iida, Y., Ilyina, T., Jacobson, A. R., Jain, A., Jarníková, T., Jersild, A., Jiang, F., Jin, Z., Joos, F., Kato, E., Keeling, R. F., Kennedy, D., Klein Goldewijk, K., Knauer, J., Korsbakken, J. I., Körtzinger, A., Lan, X., Lefèvre, N., Li, H., Liu, J., Liu, Z., Ma, L., Marland, G., Mayot, N., McGuire, P. C., McKinley, G. A., Meyer, G., Morgan, E. J., Munro, D. R., Nakaoka, S.-I., Niwa, Y., O'Brien, K. M., Olsen, A., Omar, A. M., Ono, T., Paulsen, M., Pierrot, D., Pocock, K., Poulter, B., Powis, C. M., Rehder, G., Resplandy, L., Robertson, E., Rödenbeck, C., Rosan, T. M., Schwinger, J., Séférian, R., Smallman, T. L., Smith, S. M., Sospedra-Alfonso, R., Sun, Q., Sutton, A. J., Sweeney, C., Takao, S., Tans, P. P., Tian, H., Tilbrook, B., Tsujino, H., Tubiello, F., van der Werf, G. R., van Ooijen, E., Wanninkhof, R., Watanabe, M., Wimart-Rousseau, C., Yang, D., Yang, X., Yuan, W., Yue, X., Zaehle, S., Zeng, J., and Zheng, B.: Global Carbon Budget 2023, Earth System Science Data, 15, 5301–5369, https://doi.org/10.5194/essd-15-5301-2023, 2023.

Garcia-Carreras, L., Challinor, A. J., Parkes, B. J., Birch, C. E., Nicklin, K. J., and Parker, D. J.: The Impact of Parameterized Convection on the Simulation of Crop Processes, Journal of Applied Meteorology and Climatology, 54, 1283 – 1296, https://doi.org/10.1175/JAMC-D-14-0226.1, 2015.

Georgievski, G. and Hagemann, S.: Characterizing uncertainties in the ESA-CCI land cover map of the epoch 2010 and their impacts on MPI-ESM climate simulations, Theoretical and Applied Climatology, 137, 1587–1603, 2019.

Gu, L., Baldocchi, D. D., Wofsy, S. C., Munger, J. W., Michalsky, J. J., Urbanski, S. P., and Boden, T. A.: Response of a deciduous forest to the Mount Pinatubo eruption: Enhanced photosynthesis, Science, 299, 2035–2038, 2003.

Hardouin, L., Delire, C., Decharme, B., Lawrence, D. M., Nabel, J. E., Brovkin, V., Collier, N., Fisher, R., Hoffman, F. M., Koven, C. D., et al.: Uncertainty in land carbon budget simulated by terrestrial biosphere models: the role of atmospheric forcing, Environmental Research Letters, 17, 094 033, 2022.

Hartley, A., MacBean, N., Georgievski, G., and Bontemps, S.: Uncertainty in plant functional type distributions and its impact on land surface models, Remote Sensing of Environment, 203, 71–89, https://doi.org/https://doi.org/10.1016/j.rse.2017.07.037, earth Observation of Essential Climate Variables, 2017.

Hashimoto, S., Carvalhais, N., Ito, A., Migliavacca, M., Nishina, K., and Reichstein, M.: Global spatiotemporal distribution of soil respiration modeled using a global database, Biogeosciences, 12, 4121–4132, 2015.

Hoffman, F. M., Randerson, J. T., Arora, V. K., Bao, Q., Cadule, P., Ji, D., Jones, C. D., Kawamiya, M., Khatiwala, S., Lindsay, K., et al.: Causes and implications of persistent atmospheric carbon dioxide biases in Earth System Models, Journal of Geophysical Research: Biogeosciences, 119, 141–162, 2014.

Hohenegger, C., Korn, P., Linardakis, L., Redler, R., Schnur, R., Adamidis, P., Bao, J., Bastin, S., Behravesh, M., Bergemann, M., et al.: ICON-Sapphire: simulating the components of the Earth system and their interactions at kilometer and subkilometer scales, Geoscientific Model Development, 16, 779–811, 2023.

Humphrey, V., Berg, A., Ciais, P., Gentine, P., Jung, M., Reichstein, M., Seneviratne, S. I., and Frankenberg, C.: Soil moisture–atmosphere feedback dominates land carbon uptake variability, Nature, 592, 65–69, https://doi.org/10.1038/s41586-021-03325-5, 2021.

Huntzinger, D., Schwalm, C., Michalak, A., Schaefer, K., King, A., Wei, Y., Jacobson, A., Liu, S., Cook, R., Post, W., et al.: The North American carbon program multi-scale synthesis and terrestrial model intercomparison project–Part 1: Overview and experimental design, Geoscientific Model Development, 6, 2121–2133, 2013.

Huntzinger, D., Schwalm, C., Wei, Y., Cook, R., Michalak, A., Schaefer, K., Jacobson, A., Arain, M., Ciais, P., Fisher, J., et al.: NACP MsTMIP: Global 0.5-degree Model Outputs in Standard Format, Version 1.0. ORNL DAAC, Oak Ridge, Tennessee, USA, 2018.

Jung, M., Le Maire, G., Zaehle, S., Luyssaert, S., Vetter, M., Churkina, G., Ciais, P., Viovy, N., and Reichstein, M.: Assessing the ability of three land ecosystem models to simulate gross carbon uptake of forests from boreal to Mediterranean climate in Europe, Biogeosciences, 4, 647–656, 2007a.

Jung, M., Vetter, M., Herold, M., Churkina, G., Reichstein, M., Zaehle, S., Ciais, P., Viovy, N., Bondeau, A., Chen, Y., et al.: Uncertainties of modeling gross primary productivity over Europe: A systematic study on the effects of using different drivers and terrestrial biosphere models, Global Biogeochemical Cycles, 21, 2007b.

Kang, Y., Bassiouni, M., Gaber, M., Lu, X., and Keenan, T. F.: CEDAR-GPP: spatiotemporally upscaled estimates of gross primary productivity incorporating CO_2 fertilization, Earth System Science Data, 17, 3009–3046, https://doi.org/10.5194/essd-17-3009-2025, 2025.

Knorr, W.: Satellite remote sensing and modelling of the global CO2 exchange of land vegetation: a synthesis study, Max-Planck-Institut fur Meteorologie Examensarbeit, 49, 185, 1997.

Knorr, W.: Annual and interannual CO2 exchanges of the terrestrial biosphere: Process-based simulations and uncertainties, Global ecology and biogeography, 9, 225–252, 2000.

Lazoglou, G., Economou, T., Anagnostopoulou, C., Zittis, G., Tzyrkalli, A., Georgiades, P., and Lelieveld, J.: Multivariate adjustment of drizzle bias using machine learning in European climate projections, Geoscientific Model Development, 17, 4689–4703, https://doi.org/10.5194/gmd-17-4689-2024, 2024.

Liski, J., Palosuo, T., Peltoniemi, M., and Sievanen, R.: Carbon and decomposition model Yasso for forest soils, Ecological Modelling, pp. 168–182, 2005.

Mauritsen, T., Bader, J., Becker, T., Behrens, J., Bittner, M., Brokopf, R., Brovkin, V., Claussen, M., Crueger, T., Esch, M., et al.: Developments in the MPI-M Earth System Model version 1.2 (MPI-ESM1. 2) and its response to increasing CO2, Journal of Advances in Modeling Earth Systems, 11, 998–1038, 2019.

McGuire, A. D., Melillo, J. M., Joyce, L., Kicklighter, D. W., Grace, A., Moore III, B., and Vorosmarty, C. J.: Interactions between carbon and nitrogen dynamics in estimating net primary productivity for potential vegetation in North America, Global Biogeochemical Cycles, 6, 101–124, 1992.

Morales, P., Hickler, T., Rowell, D. P., Smith, B., and Sykes, M. T.: Changes in European ecosystem productivity and carbon balance driven by regional climate model output, Global Change Biology, 13, 108–122, 2007.

Müller, C., Eickhout, B., Zaehle, S., Bondeau, A., Cramer, W., and Lucht, W.: Effects of changes in CO2, climate, and land use on the carbon balance of the land biosphere during the 21st century, Journal of Geophysical Research: Biogeosciences, 112, 2007.

Nemani, R. R., Keeling, C. D., Hashimoto, H., Jolly, W. M., Piper, S. C., Tucker, C. J., Myneni, R. B., and Running, S. W.: Climate-driven increases in global terrestrial net primary production from 1982 to 1999, science, 300, 1560–1563, 2003.

Pastorello, G., Trotta, C., Canfora, E., Chu, H., Christianson, D., Cheah, Y.-W., Poindexter, C., Chen, J., Elbashandy, A., Humphrey, M., et al.: The FLUXNET2015 dataset and the ONEFlux processing pipeline for eddy covariance data, Scientific data, 7, 225, 2020.

Prein, A. F., Langhans, W., Fosser, G., Ferrone, A., Ban, N., Goergen, K., Keller, M., Tölle, M., Gutjahr, O., Feser, F., et al.: A review on regional convection-permitting climate modeling: Demonstrations, prospects, and challenges, Reviews of geophysics, 53, 323–361, 2015.

Pu, J., Chang, Y., Gao, S., Bao, S., Yan, K., Sun, X., Carvalhais, N., and Myneni, R. B.: MCI GPP: ensembling a global model- and climate-independent gross primary productivity for 2001–2023, Scientific Data, 12, 1965, https://doi.org/10.1038/s41597-025-06218-8, 2025.

Qian, H., Joseph, R., and Zeng, N.: Enhanced terrestrial carbon uptake in the Northern High Latitudes in the 21st century from the Coupled Carbon Cycle Climate Model Intercomparison Project model projections, Global Change Biology, 16, 641–656, 2010.

Running, S. and Zhao, M.: MODIS/Terra gross primary productivity gap-filled 8-day L4 global 500m SIN grid V061, NASA EOSDIS Land Processes Distributed Active Archive Center (DAAC) data set, pp. MOD17A2HGF–061, 2021.

Schaphoff, S., Lucht, W., Gerten, D., Sitch, S., Cramer, W., and Prentice, I. C.: Terrestrial biosphere carbon storage under alternative climate projections, Climatic change, 74, 97–122, 2006.

Schär, C., Fuhrer, O., Arteaga, A., Ban, N., Charpilloz, C., Di Girolamo, S., Hentgen, L., Hoefler, T., Lapillonne, X., Leutwyler, D., et al.: Kilometer-scale climate models: Prospects and challenges, Bulletin of the American Meteorological Society, 101, E567–E587, 2020.

Schneck, R., Gayler, V., Nabel, J. E., Raddatz, T., Reick, C. H., and Schnur, R.: Assessment of JSBACHv4. 30 as a land component of ICON-ESM-V1 in comparison to its predecessor JSBACHv3. 2 of MPI-ESM1. 2, Geoscientific Model Development, 15, 8581–8611, 2022.

Segura, H., Pedruzo-Bagazgoitia, X., Weiss, P., Müller, S. K., Rackow, T., Lee, J., Dolores-Tesillos, E., Benedict, I., Aengenheyster, M., Aguridan, R., et al.: nextGEMS: entering the era of kilometer-scale Earth system modeling, EGUsphere, 2025, 1–39, 2025.

Stevens, B., Acquistapace, C., Hansen, A., Heinze, R., Klinger, C., Klocke, D., Rybka, H., Schubotz, W., Windmiller, J., Adamidis, P., Arka, I., Barlakas, V., Biercamp, J., Brueck, M., Brune, S., Buehler, S. A., Burkhardt, U., Cioni, G., Costa-Suros, M., Crewell, S., Crueger, T., Deneke, H., Friederichs, P., Henken, C. C., Hohenegger, C., Jacob, M., Jakub, F., Kalthoff, N., Koehler, M., van Laar, T. W., Li, P., Loehnert, U., Macke, A., Madenach, N., Mayer, B., Nam, C., Naumann, A. K., Peters, K., Poll, S., Quaas, J., Roeber, N., Rochetin, N., Scheck, L., Schemann, V., Schnitt, S., Seifert, A., Senf, F., Shapkalijevski, M., Simmer, C., Singh, S., Sourdeval, O., Spickermann, D., Strandgren, J., Tessiot, O., Vercauteren, N., Vial, J., Voigt, A., and Zaengl, G.: The Added Value of Large-eddy and Storm-resolving Models for Simulating Clouds and Precipitation, Journal of the Meteorological Society of Japan, pp. 395–435, 2020.

Store, C. C. D.: Land cover classification gridded maps from 1992 to present derived from satellite observations, Copernicus Climate Change Service, pp. 7–9, 2019.

Sun, Y., Solomon, S., Dai, A., and Portmann, R.: How often does it rain?, 2005.

Tang, X., Fan, S., Du, M., Zhang, W., Gao, S., Liu, S., Chen, G., Yu, Z., and Yang, W.: Spatial and temporal patterns of global soil heterotrophic respiration in terrestrial ecosystems, Earth System Science Data, 12, 1037–1051, 2020.

Tuomi, M., Thum, T., Järvinen, H., Fronzek, S., Berg, B., Harmon, M., Trofymow, J., Sevanto, S., and Liski, J.: Leaf litter decomposition—Estimates of global variability based on Yasso07 model, Ecological Modelling, 220, 3362–3371, 2009.

Vetter, M., Churkina, G., Jung, M., Reichstein, M., Zaehle, S., Bondeau, A., Chen, Y., Ciais, P., Feser, F., Freibauer, A., et al.: Analyzing the causes and spatial pattern of the European 2003 carbon flux anomaly using seven models, Biogeosciences, 5, 561–583, 2008.

Wieners, K.-H., Giorgetta, M., Jungclaus, J., Reick, C., Esch, M., Bittner, M., Gayler, V., Haak, H., de Vrese, P., Raddatz, T., Mauritsen, T., von Storch, J.-S., Behrens, J., Brovkin, V., Claussen, M., Crueger, T., Fast, I., Fiedler, S., Hagemann, S., Hohenegger, C., Jahns, T., Kloster, S., Kinne, S., Lasslop, G., Kornblueh, L., Marotzke, J., Matei, D., Meraner, K., Mikolajewicz, U., Modali, K., Müller, W., Nabel, J., Notz, D., Peters-von Gehlen, K., Pincus, R., Pohlmann, H., Pongratz, J., Rast, S., Schmidt, H., Schnur, R., Schulzweida, U., Six, K., Stevens, B., Voigt, A., and Roeckner, E.: MPI-M MPI-ESM1.2-LR model output prepared for CMIP6 ScenarioMIP ssp245, https://doi.org/10.22033/ESGF/CMIP6.6693, 2019.

Yuan, Q., Wang, X., Che, T., and Li, J.: Global carbon flux dataset generated by fusing remote sensing and multiple flux networks observation, Scientific Data, 12, 1359, https://doi.org/10.1038/s41597-025-05672-8, 2025.

Zhang, Y., Bastos, A., Maignan, F., Goll, D., Boucher, O., Li, L., Cescatti, A., Vuichard, N., Chen, X., Ammann, C., et al.: Modeling the impacts of diffuse light fraction on photosynthesis in ORCHIDEE (v5453) land surface model, Geoscientific Model Development Discussions, 2020, 1–35, 2020.

Zhu, S., Xu, J., Zeng, J., Bao, S., Chen, Y., Shi, S., Zheng, Z., Dong, W., Wang, Y., and Shi, J.: The UFLUX ensemble of multiple-scale carbon, water, and energy fluxes, Scientific Data, 13, 90, https://doi.org/10.1038/s41597-025-06401-x, 2025.